

## Article

# MAPLE Coatings Embedded with Essential Oil-Conjugated Magnetite for Anti-Biofilm Applications

Oana Gherasim <sup>1,2</sup>, Roxana Cristina Popescu <sup>3</sup>, Valentina Grumezescu <sup>2,\*</sup>, George Dan Mogosanu <sup>4</sup> , Laurențiu Mogoantă <sup>5</sup>, Florin Iordache <sup>6</sup> , Alina Maria Holban <sup>7,8</sup>, Bogdan Stefan Vasile <sup>1</sup> , Alexandra Cătălina Bîrcă <sup>1</sup>, Ovidiu-Cristian Oprea <sup>9</sup> , Alexandru Mihai Grumezescu <sup>1,8</sup>  and Ecaterina Andronescu <sup>1</sup> 

<sup>1</sup> Department of Science and Engineering of Oxide Materials and Nanomaterials, Faculty of Applied Chemistry and Materials Science, Politehnica University of Bucharest, 1-7 Gheorghe Polizu Street, 011061 Bucharest, Romania; oana.gherasim@inflpr.ro (O.G.); bogdan.vasile@upb.ro (B.S.V.); ada\_birca@yahoo.com (A.C.B.); grumezescu@yahoo.com (A.M.G.); ecaterina.andronescu@upb.ro (E.A.)

<sup>2</sup> Lasers Department, National Institute for Lasers, Plasma and Radiation Physics, 409 Atomistilor Street, 077125 Magurele, Romania

<sup>3</sup> Department of Life and Environmental Physics, “Horia Hulubei” National Institute for Physics and Nuclear Engineering, 30 Reactorului Street, 077125 Magurele, Romania; roxana.popescu@nipne.ro

<sup>4</sup> Department of Pharmacognosy and Phytotherapy, Faculty of Pharmacy, University of Medicine and Pharmacy of Craiova, 2 Petru Rares Street, 200349 Craiova, Romania; mogosanu2006@yahoo.com

<sup>5</sup> Research Center for Microscopic Morphology and Immunology, University of Medicine and Pharmacy of Craiova, 2 Petru Rares Street, 200349 Craiova, Romania; laurentiu\_mogoanta@yahoo.com

<sup>6</sup> Department of Biochemistry, Faculty of Veterinary Medicine, University of Agronomic Science and Veterinary Medicine, 59 Marasti Boulevard, 011464 Bucharest, Romania; floriniordache84@yahoo.com

<sup>7</sup> Department of Microbiology and Immunology, Faculty of Biology, University of Bucharest, 91-95 Splaiul Independentei Street, 077206 Bucharest, Romania; alina\_m\_h@yahoo.com

<sup>8</sup> Research Institute of the University of Bucharest—ICUB, University of Bucharest, 90-92 Panduri Road, 050657 Bucharest, Romania

<sup>9</sup> Department of Inorganic Chemistry, Physical Chemistry and Electrochemistry, Faculty of Applied Chemistry and Materials Science, Politehnica University of Bucharest, 1-7 Gheorghe Polizu Street, 011061 Bucharest, Romania; ovidiu.oprea@upb.ro

\* Correspondence: valentina.grumezescu@inflpr.ro



**Citation:** Gherasim, O.; Popescu, R.C.; Grumezescu, V.; Mogoșanu, G.D.; Mogoantă, L.; Iordache, F.; Holban, A.M.; Vasile, B.Ş.; Bîrcă, A.C.; Oprea, O.-C.; et al. MAPLE Coatings Embedded with Essential Oil-Conjugated Magnetite for Anti-Biofilm Applications. *Materials* **2021**, *14*, 1612. <https://doi.org/10.3390/ma14071612>

Academic Editor: Luigi Calabrese

Received: 22 February 2021

Accepted: 19 March 2021

Published: 25 March 2021

**Publisher’s Note:** MDPI stays neutral with regard to jurisdictional claims in published maps and institutional affiliations.

**Abstract:** The present study reports on the development and evaluation of nanostructured composite coatings of poly(lactic acid) (PLA) embedded with iron oxide nanoparticles ( $\text{Fe}_3\text{O}_4$ ) modified with Eucalyptus (*Eucalyptus globulus*) essential oil. The co-precipitation method was employed to synthesize the magnetite particles conjugated with Eucalyptus natural antibiotic ( $\text{Fe}_3\text{O}_4@\text{EG}$ ), while their composition and microstructure were investigated using grazing incidence X-ray diffraction (GIXRD), Fourier transform infrared spectroscopy (FT-IR), thermogravimetric analysis (TGA), transmission electron microscopy (TEM) and dynamic light scattering (DLS). The matrix-assisted pulsed laser evaporation (MAPLE) technique was further employed to obtain PLA/ $\text{Fe}_3\text{O}_4@\text{EG}$  thin films. Optimal experimental conditions for laser processing were established by complementary infrared microscopy (IRM) and scanning electron microscopy (SEM) investigations. The in vitro biocompatibility with eukaryote cells was proven using mesenchymal stem cells, while the anti-biofilm efficiency of composite PLA/ $\text{Fe}_3\text{O}_4@\text{EG}$  coatings was assessed against Gram-negative and Gram-positive pathogens.

**Keywords:** magnetite; essential oil; MAPLE; composite coatings; anti-biofilm efficiency

## 1. Introduction

Traditional medicine relies on exploring the experience-based therapeutic benefits of extracts and infusions from different parts of plants and herbs. However, this rather temporary and non-selective approach and the current advances in pharmaceutical sciences determined an increased interest for new and performance-enhanced formulations. The

intrinsic medicinal properties of phytochemicals have been acknowledged for a long period of time [1,2], but the interest for such natural-derived bioactive substances has lately grown considerably [3–10].

Given the actual context of alarming increasing prevalence of antibiotic-resistant bacteria [11,12], particular attention was oriented on developing new antimicrobial formulations. For example, extracts of acacia gum [13,14], cinnamon [15,16], clove [17,18], cumin [19,20], lavender [21,22], oregano [23,24], rosemary [25,26], sage [27,28], tea tree [29,30] and thyme [31,32] were reported as promising alternatives to combat the growth of planktonic microorganisms, as well as the formation and development of bacterial biofilms.

Substantial antibacterial effects of Eucalyptus essential oils were evidenced against *Escherichia coli* and *Staphylococcus aureus* by Bachir & Benali, with a more prominent effect being reported on the Gram-negative strain [33]. The increased efficiency of essential oils derived from different Eucalyptus species against Gram-negative pathogens [34,35] was mainly related to the abundance of a water-insoluble 1,8-cineole (eucalyptol) component, which may cause the disruption of bacterial outer membrane and the leakage of cytoplasm [36,37]. Complementary studies evaluated the correlation between the chemical composition and the antibacterial efficiency of essential oils from different Eucalyptus species, proving their potential application in pharmaceutical products [38,39].

To reach the required therapeutic concentrations, high doses from traditional pharmaceutical formulations are usually administered. Modern drug delivery systems represent an attractive, versatile and effective approach to overcome the limitations of regular medicines, such as: (i) side effects; (ii) poor drug concentration at the targeted place; (iii) the rapid metabolizing rate; and (iv) the degradation of active substances.

By gathering the great outcome of nanotechnology and the therapeutic implications of plant-derived compounds, new pharmaceutical formulations were lately developed and thoroughly evaluated. Therefore, an impressive extension of the medicinal use of phytochemicals was reported, including unconventional antioxidants [40–44] and antimicrobials [45–48], wound dressings [49–51], dermal products [52–55] and anti-cancer platforms [56–59].

A particular application of nanotechnology-derived unconventional formulations consists of optimizing the surface of commonly used medical devices with nanostructured and bioactive coatings, intending to potentiate or induce anti-infective properties [60–62]. The development of antimicrobial and anti-biofilm coatings that combat drug-resistant microorganisms and reduce or eliminate related infections is of great interest for the healthcare system.

Magnetite ( $\text{Fe}_3\text{O}_4$ ) is the most explored representative of iron oxides, with remarkable implications for biomedical use [63–65]. Besides facile and significant yield synthesis,  $\text{Fe}_3\text{O}_4$  particles possess peculiar nanosize-related features, such as surface functionalization, tunable biocompatibility and superparamagnetic behavior [66–70]. The surface modification of magnetite nanoparticles with essential oils represents a bidirectional strategy to obtain multifunctional platforms: (i) firstly, the organic molecules act as modulators for the compatibility and stability of  $\text{Fe}_3\text{O}_4$  nanoparticles; and (ii) secondly, the inorganic core acts as a stabilizer and potentiating agent for the essential oils [71,72]. By combining these benefits, new and effective therapeutic nanosystems can be provided, with the additional ability of targeted and controlled treatment.

For this reason, we report herein the deposition of composite films based on polylactic acid (PLA) embedded with magnetite nanoparticles *in situ* conjugated with Eucalyptus essential oil ( $\text{Fe}_3\text{O}_4@\text{EG}$ ). The chemical co-precipitation method employed in the study offers a high yield reaction and reproducibility in the synthesis of Eucalyptus-conjugated nanoparticles. The embedding of  $\text{Fe}_3\text{O}_4@\text{EG}$  systems within polymeric films of PLA was done to protect the active substance, improve the system's biocompatibility, implement a slow release of the active substance, and protect the considered medical device of eventual oxidation and degradation processes. Given the promising data on the matrix-assisted pulsed laser evaporation (MAPLE) method towards the fabrication of bioactive,

stoichiometric and homogenous coatings [73,74], this technique was used in order to obtain nanostructured PLA/Fe<sub>3</sub>O<sub>4</sub>@EG surfaces.

## 2. Materials and Methods

### 2.1. Materials

All reagents used to synthesize nanosystems, and nanostructured coatings were acquired from Sigma-Aldrich (Merck Group, Darmstadt, Germany), if not specified. All chemicals were characterized by analytical purity, according to the American Chemical Society (ACS), and all solutions were prepared using deionized water (MiliQ®, Merck Millipore, Burlington, MA, SUA).

*Eucalyptus globulus* (EG) essential oil and 1 cm<sup>2</sup> polished (1 0 0) silicon (Si) and glass substrates were provided by a local supplier.

Cell cultures, i.e., human mesenchymal stem cells derived from amniotic fluid and bacterial strains of *Escherichia coli* (ATCC® 15224) and *Staphylococcus aureus* (ATCC® 25923), were obtained from the American Type Culture Collection (ATCC, Manassas, VA, USA).

### 2.2. Methods

#### 2.2.1. Synthesis of Fe<sub>3</sub>O<sub>4</sub>@EG Nanoparticles

Magnetite nanoparticles conjugated with Eucalyptus essential oil (Fe<sub>3</sub>O<sub>4</sub>@EG) were obtained using a modified chemical co-precipitation method, in compliance with previous studies [75,76]. In this respect, metallic precursor solution was obtained by dissolving ferric chloride (FeCl<sub>3</sub>) and ferrous sulfate (FeSO<sub>4</sub>·7H<sub>2</sub>O) in MiliQ. The resulted solution was subsequently added drop by drop within an alkaline solution consisting of 25% ammonium hydroxide (NH<sub>3</sub>·OH), EG essential oil and MiliQ. The process was completed under magnetic stirring, and the resulted precipitate was washed several times with deionized water under magnetic separation. The final product was dried at 40 °C for 6 h, under an inert atmosphere.

#### 2.2.2. Synthesis of PLA/Fe<sub>3</sub>O<sub>4</sub>@EG Coatings

Before MAPLE processing, all substrates were subsequently cleaned for 30 min with acetone, ethanol and MiliQ in an ultrasonic bath, then dried under a high-purity nitrogen jet. The solid MAPLE targets were prepared by freezing at liquid nitrogen temperature the suspension obtained by mixing poly(D,L-lactide) (PLA) and Fe<sub>3</sub>O<sub>4</sub>@EG in dimethyl sulfoxide (DMSO).

The as-obtained frozen targets were further irradiated with a KrF\* excimer laser beam ( $\lambda = 248$  nm,  $\tau_{FWHM} = 25$  ns), using a COMPexPro 205 Lambda Physics source from Coherent (Göttingen, Germany). During MAPLE processing, experimental parameters were set as follows: room temperature and 0.1 Pa pressure inside the deposition chamber, 4 cm target-to-substrate distance, 0.4 Hz and 15 Hz target rotation and laser repetition frequency, respectively. 30,000 laser pulses were applied at different fluences (200, 300 and 400 mJ/cm<sup>2</sup>) to obtain PLA/Fe<sub>3</sub>O<sub>4</sub>@EG coatings.

#### 2.2.3. Physiochemical Characterization

##### X-Ray Diffraction (XRD)

To investigate the purity and crystallinity of synthesized powdery sample, grazing incidence XRD analysis was performed using a PANalytical Empyrean diffractometer (Almelo, the Netherlands) with CuK $\alpha$  radiation ( $\lambda = 1.541874$  Å), equipped with a 2 × GE (2 2 0) hybrid monochromator for Cu and a parallel plate collimator on the PIXcel3D detector. The scanning was done for 2θ diffraction angles in the 20–80° range, with an incidence angle of 0.5°, a step dimension of 0.04° and a time step of 3 s.

##### Fourier Transform Infrared Spectroscopy (FT-IR)

Compositional aspects on the synthesized powder were obtained using a Nicolet 6700 FT-IR spectrometer (Thermo Fischer Scientific, Waltham, MA, USA) connected to

the OmnicPicta 8.2 software. To get the FT-IR spectrum, 32 scans were recorded in the 4000–400  $\text{cm}^{-1}$  frequency range, with 4  $\text{cm}^{-1}$  resolution. Scanning was done under a controlled ambient temperature in the attenuated total reflectance mode.

#### Thermogravimetric Analysis (TGA)

The thermal behavior of pristine and EG-conjugated iron oxide powders was investigated using Shimadzu DTG-TA-50H equipment (Carlsbad, CA, USA). Small amounts of powdery samples were placed in alumina crucibles, heated from room temperature to 1000 °C with a heating rate of 1 °C/min, in a normal atmosphere.

#### Transmission Electron Microscopy (TEM)

Relevant microstructural data on the synthesized particles were provided by TEM analysis, which was performed with a Tecnai<sup>TM</sup> G2 F30 S-TWIN instrument equipped with a selected area electron diffraction (SAED) accessory (FEI Company, Thermo Fisher Scientific, Hillsboro, OR, USA). The microscope was used in the transmission mode, at a 300 kV voltage, with point and line resolutions of 2 Å and 1 Å, respectively. For analysis, serial ethanol dilutions were obtained, and the final suspension was placed on a holey carbon-copper grid for investigation.

#### Dynamic Light Scattering (DLS)

The hydrodynamic diameter and zeta potential of EG-conjugated particles were determined using a DelsaMax Pro instrument from Beckman Coulter (Brea, CA, USA). Prior to the analysis (performed with a 532 nm laser beam), ultrapure water dilution was prepared by ultrasound dispersion at room temperature.

#### Infrared Microscopy (IRM)

Relevant compositional information on the MAPLE processed materials was provided by IRM analysis, which was made using a Nicolet iN10 MX FT-IR microscope (Thermo Fisher Scientific Company, Waltham, MA, USA). Measurements were recorded between 4000 and 700  $\text{cm}^{-1}$  at 4  $\text{cm}^{-1}$  resolution, in the reflection mode. Thirty-two scans were collected for each sample, then co-added and converted to absorbance using the OmnicPicta 8.0 software (Thermo Fisher Scientific).

#### Scanning Electron Microscopy (SEM)

A FEI Quanta Inspect F scanning electron microscope (Thermo Fisher Scientific, Hillsboro, OR, USA) was used to evaluate the morphology of PLA/Fe<sub>3</sub>O<sub>4</sub>@EG films. Prior to analysis, samples were capped with a thin gold layer and the SEM micrographs were recorded using secondary electron beams (energy of 30 keV). For cross-section investigation, the (1 0 0) Si substrates used during MAPLE processing were cut with a diamond disc.

#### 2.2.4. In Vivo Biodistribution of Fe<sub>3</sub>O<sub>4</sub>@EG Nanoparticles

To evaluate the in vivo effects of Fe<sub>3</sub>O<sub>4</sub>@EG nanosystems, suspensions were prepared in phosphate-buffered saline (1 mg/mL concentration) and subjected to UV treatment (30 min). Volumes of 100  $\mu\text{L}$  from as-obtained sterile suspensions were aseptically administered into the left jugular vein of three-weeks-old BALB/c mice, under general anesthesia (Ketamine/Xylazine mixture). Reference mice were injected with 100  $\mu\text{L}$  of phosphate-buffered saline (PBS). After inoculation, all animals were kept in standard conditions and received food and water *ad libitum*.

After 2 days and 10 days of treatment, animals were euthanized under general anesthesia, and internal organs (brain, myocardium, liver, lung, pancreas, kidney and spleen) were harvested. The harvested organs were washed with PBS, preserved in 10% buffered neutral formalin (72 h, room temperature) and prepared for paraffin processing. Serial cross-sections of 4  $\mu\text{m}$  thickness were cut using an HM355s rotary microtome equipped

with a waterfall-based section transfer system (MICROM International GmbH, Walldorf, Germany). The as-obtained tissue fragments were placed on histological slides, treated with poly-L-Lysine and the classical Hematoxylin–Eosin (HE) staining protocol was applied. Cross-section tissue samples were examined and photographed with a Nikon Eclipse 55i light microscope coupled with a Nikon DS-Fi1 CCD high definition video camera from Nikon Instruments (Apidrag, Bucharest, Romania). Optical micrographs were captured, stored and processed using the Image-Pro Plus 7.0.0 software from Media Cybernetics Inc. (Buckinghamshire, UK).

Animal experiments within this study were performed in compliance with all European Commission directives on animal experiments and were approved by the Ethics Committee of the University of Medicine and Pharmacy of Craiova, Romania.

#### 2.2.5. In Vitro Evaluation of PLA/Fe<sub>3</sub>O<sub>4</sub>@EG Coatings

##### Biocompatibility Evaluation

The biocompatibility of composite materials was quantitatively assessed on amniotic fluid-derived mesenchymal stem cells (AFSCs) using the MTT tetrazole (3-(4,5-dimethylthiazol-2-yl)-2,5-diphenyltetrazolium bromide) viability assay. For biological evaluation, reduced amounts of PLA/Fe<sub>3</sub>O<sub>4</sub>@EG were obtained by scratching an area of 0.25 cm<sup>2</sup> from the MAPLE-coated glass substrates. All samples were sterilized using UV irradiation.

AFSCs were seeded at 3000 cells/well cellular densities in 100 µl of Dulbecco's Modified Eagle Medium supplemented with 10% fetal bovine serum and 1% antibiotic mixture (Penicillin/Streptomycin/Neomycin), using 96-well plates (Thermo Fisher Scientific, Waltham, MA, USA). After 72h of standard incubation (37 ± 2 °C, 5 ± 1% CO<sub>2</sub>, humid atmosphere), the viability of cells was quantitatively determined using the Vybrant® MTT Cell Proliferation Assay Kit (Thermo Fischer Scientific). Two supplementary dark incubation periods (4h each) were required after the addition of 10 µL of 12 mM MTT solution and 100 µL of SDS-HCl solubilizing solution in each well, respectively. The absorbance values for each specimen were spectrophotometrically measured at 570 nm, using in this respect a Mithras LB 940 instrument (Berthold Technology, Bad Wildbad, Germany). The MTT viability assay was performed in triplicate experiments at different time intervals.

##### Anti-Adherent Potential

The ability of PLA/Fe<sub>3</sub>O<sub>4</sub>@EG materials to interfere with the development of bacterial biofilms of *Escherichia coli* (*E. coli*) and *Staphylococcus aureus* (*S. aureus*) was experimentally evaluated. All samples (uncoated and MAPLE modified glass substrates) were sterilized using 20 min of UV irradiation. Each sample was individually placed in wells of a 6-well plate (Nunc), followed by the addition of 2 mL of Luria-Bertani (LB) broth and subsequent inoculation of 50 µL of microbial suspensions (0.5 McFarland standard densities). After 24h of incubation in standard conditions, the samples were washed with sterile physiological PBS, the culture medium was removed and fresh LB medium was added to ensure the growth of microbial biofilm. After 24, 48 and 72 h of incubation, specimens were washed with PBS and placed into PBS-containing sterile tubes for subsequent vortexing (30 s). The biofilm-forming cell suspensions were diluted and seeded onto solidified LB agar plates in order to evaluate the colony-forming units (CFU/mL). All experiments were performed in triplicate.

### 3. Results & Discussions

For the synthesis of conjugated iron oxide nanoparticles, we used a modified chemical co-precipitation method, which implied using Fe<sup>2+</sup>:Fe<sup>3+</sup> in a 1.6:1 ratio. The contribution of trivalent cation was smaller to compensate the oxidation of Fe<sup>2+</sup> [77,78], while the precipitation condition was provided by properly adjusting the pH value around 11 with a weak alkaline solution. The organic phase (Eucalyptus essential oil) was introduced in the precipitation medium to form micelles, limiting the nucleation stage of nanoparticles

and ensuring a better control of their growth and dimension [79,80]. The molecules of EG essential oil also acted as an *in situ* functionalizing agent by establishing weak interactions with the abundant hydroxyl groups on the surface of nanoparticles [81,82]. The synthesized iron oxide powder was subjected to characterization by means of composition, crystallinity and morphology.

The XRD pattern (Figure 1) shows the presence of strong diffraction interferences that are characteristic for one mineralogical phase, namely magnetite ( $\text{Fe}_3\text{O}_4$ ), as identified from the ICDD (International Centre of Diffraction Data) card No. 19-0629. Six specific diffraction planes corresponding to  $2\theta$  values of  $\sim 30^\circ$ ,  $\sim 35^\circ$ ,  $\sim 43^\circ$ ,  $\sim 53^\circ$ ,  $\sim 57^\circ$  and  $\sim 62^\circ$  ( $^\circ$ ) were thus identified, namely (2 2 0), (3 1 1), (4 0 0), (4 2 2), (5 1 1) and (4 4 0). The results are in concordance with previously reported data [83,84] on crystalline magnetite with a spinel cubic structure.

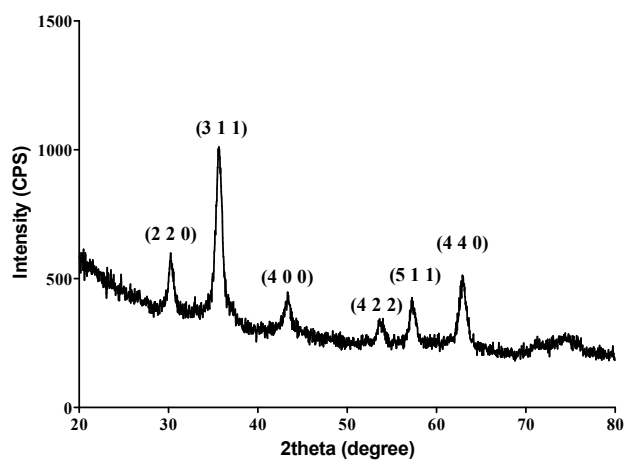


**Figure 1.** XRD pattern of  $\text{Fe}_3\text{O}_4@\text{EG}$  particles.

The IR spectrum from Figure 2 demonstrates the successful conjugation of EG molecules onto  $\text{Fe}_3\text{O}_4$  particles. The vibrational bands identified at  $\sim 2928 \text{ cm}^{-1}$  and  $\sim 2848 \text{ cm}^{-1}$  correspond to the asymmetric and symmetric stretching of  $-\text{CH}_3$  originating from Eucalyptus essential oil [85], while the  $\sim 558 \text{ cm}^{-1}$  band is assigned to Fe–O stretching vibrations from magnetite [86,87].

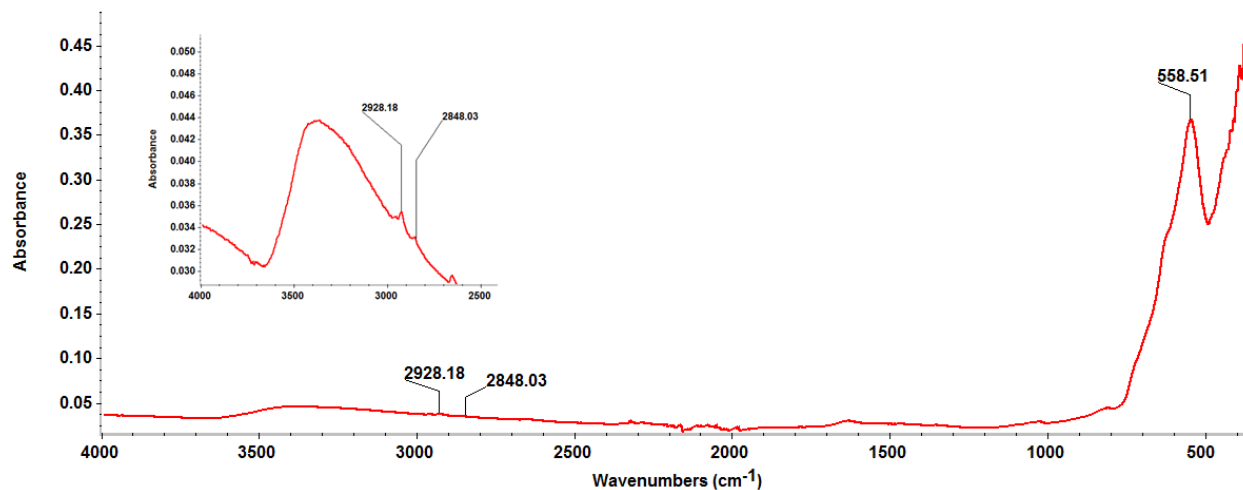


**Figure 2.** Fourier transform infrared spectroscopy (FT-IR) spectrum of  $\text{Fe}_3\text{O}_4@\text{EG}$  particles.

To obtain qualitative and quantitative information on the composition of synthesized particles, comparative thermal studies (Figure 3) on pristine and EG-conjugated  $\text{Fe}_3\text{O}_4$  were performed, using in this respect TGA and differential scanning calorimetry (DSC). The

derivatogram corresponding to bare  $\text{Fe}_3\text{O}_4$  evidences a total weight loss of 2.81%, which occurred in three steps: (i) the first weight loss, accompanied by an exothermic process, is recorded at 139.2 °C, and is attributed to the evaporation of water adsorbed on the surface of particles (water chemo-desorption); (ii) the second exothermic event (between 300–400 °C) has a lower amplitude, but is correlated with a reduction in the sample's mass of 1.27%, which may be due to the elimination of absorbed water molecules as a result of the complete degradation of hydroxyl groups from the surface of iron oxide nanoparticles; and (iii) the last exothermic phenomenon comes together with a mass change of 0.73%, and may be attributed to the isomorphic transformation of magnetite into  $\gamma$ -maghemite [88,89].

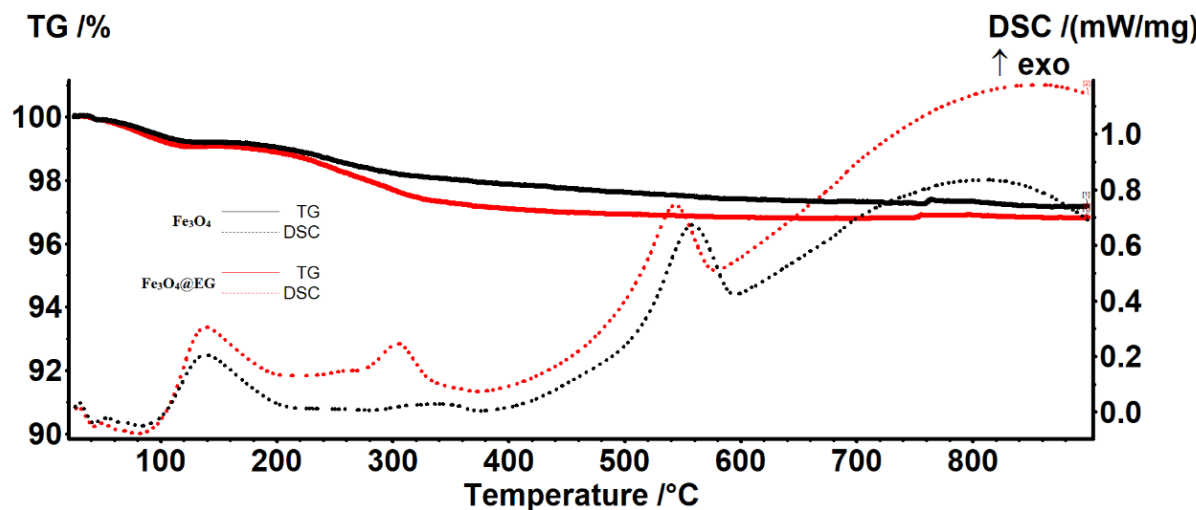


**Figure 3.** Thermal analysis of  $\text{Fe}_3\text{O}_4$  and  $\text{Fe}_3\text{O}_4@\text{EG}$  particles.

In the case of  $\text{Fe}_3\text{O}_4@\text{EG}$  sample, a similar thermal behavior pattern was followed: there are three main exothermic events, accompanied by mass reductions. In comparison with the pristine iron oxide sample, the amplitude of the process that occurred at ~300 °C is much higher and comes together with an increased mass reduction (1.92%). This may result from the degradation of the organic molecules from Eucalyptus essential oil, which were conjugated onto the nanoparticles' surface during the synthesis process. A total mass loss of 3.17% is noticed for the  $\text{Fe}_3\text{O}_4@\text{EG}$  sample. By considering both powdery samples' thermal data, we can estimate the amount of EG essential oil as  $0.36 \pm 0.1$  wt.%.

Relevant microstructural aspects on the  $\text{Fe}_3\text{O}_4@\text{EG}$  particles were provided by transmission electron micrographs (Figure 4). A pronounced agglomeration tendency of the powdery sample is noticed (Figure 4a), together with the presence of individual nanoparticles that possess no preferential morphology and a non-homogenous aspect. A complementary micrograph (Figure 4b) indicates the quasi-spherical morphology of  $\text{Fe}_3\text{O}_4@\text{EG}$  particles and confirms their nanosize (average diameter of  $7.5 \pm 2.5$  nm). It can also be noticed that the nanoparticles have a good dispersion in alcoholic suspension due to the stabilizing role provided by the phytochemical molecules contained in the EG essential oil. The high-resolution TEM micrograph (Figure 4c) emphasizes a preferential core/shell structure of the synthesized  $\text{Fe}_3\text{O}_4@\text{EG}$  systems, as inorganic nanoparticles of high crystallinity are individually dispersed in low crystalline organic mass. The SAED pattern of EG-conjugated nanoparticles (Figure 4c, inset) confirms the highly crystalline nature of obtained systems, while the identified diffraction planes enable us to categorize the sample as face-centered spinel structured magnetite. These results are in concordance with previously reported data [90,91], and with the above-discussed XRD results. Complementary results evidenced that  $\text{Fe}_3\text{O}_4@\text{EG}$  nanoparticles have hydrodynamic diameters between 200.9 and 247 nm, with negative surface charge ( $-1.7$  mV zeta potential).

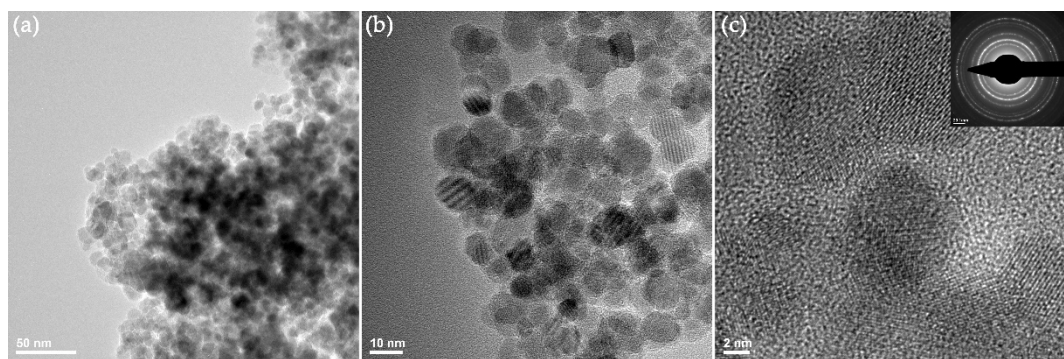


**Figure 4.** Transmission electron microscopy (TEM) (a,b) and HR-TEM (c) micrographs, and selected area electron diffraction (SAED) pattern (inset) of  $\text{Fe}_3\text{O}_4@\text{EG}$  particles.

Preferential tissue retention of  $\text{Fe}_3\text{O}_4@\text{EG}$  particles was evidenced after systemic administration and histological evaluation. No morphological alterations, ultrastructural modifications or foreign systems were observed for the brain, myocardium and pancreas tissues, regardless of the treatment period. In comparison, dark-brown aggregates were noticed within capillaries and tissue-specific macrophages of liver and lung (hepatic stellate and pulmonary perivascular macrophages, respectively), at two days after inoculation. The presence of reduced-in-size aggregates was also noticed at the renal level, but only in the blood vessels, as they were absent in glomeruli, renal tubules and renal stroma. Still, no histological alterations were observed in neither of these tissues. After a prolonged treatment (10 days) with proposed nanosystems, the liver, lung and kidney were negative for the presence of  $\text{Fe}_3\text{O}_4@\text{EG}$  nanoparticles (no ultrastructural modifications or functional alterations were identified) (Figure 5).

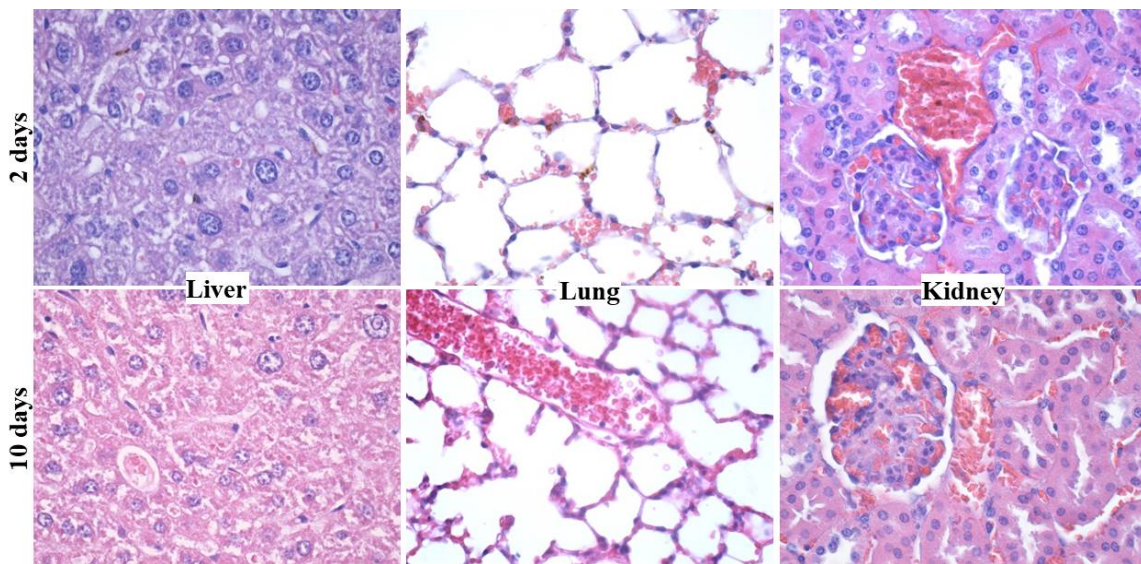


**Figure 5.** Optical micrographs of hepatic, pulmonary and renal tissues harvested after 2 and 10 days of treatment with  $\text{Fe}_3\text{O}_4@\text{EG}$  ( $400\times$  magnification).

In the case of splenic tissue (Figure 6), nanoparticle-based aggregates were evidenced in the red pulp, with higher tissue concentration at 10 days after injection.  $\text{Fe}_3\text{O}_4@\text{EG}$  were absent in the white pulp of the spleen, regardless of the applied treatment. Instead, the splenic white pulp's time-dependent hypertrophy was observed due to overstimulated production of multilobed nucleated macrophages, a process activated by the EO-conjugated magnetite nanoparticles.

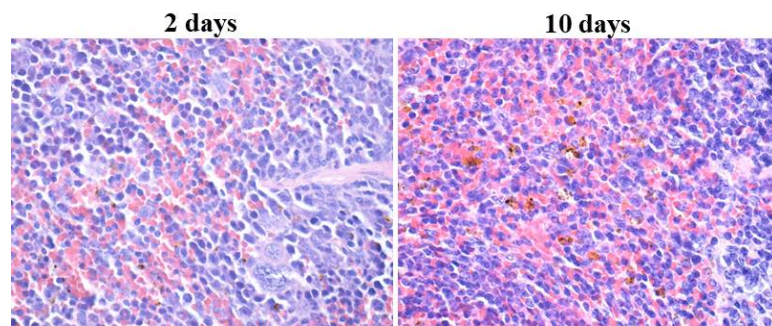


**Figure 6.** Optical micrographs of splenic tissue harvested after 2 and 10 days of treatment with  $\text{Fe}_3\text{O}_4@\text{EG}$  ( $400\times$  magnification).

The MAPLE technique gained a lot of attention for the development of biocompatible and biomimetic coatings for implantable materials and devices, thanks to its properties, such as controlled topography of resulted nanosized layers, strong adhesion between synthesized films and implant's surface, and stoichiometric transfer of target materials onto the substrates [92]. Herein, we employed this versatile laser processing method to obtain composite PLA/ $\text{Fe}_3\text{O}_4@\text{EG}$  thin films at different laser fluences (200, 300 and  $400 \text{ mJ/cm}^2$ ).

To identify optimal parameters for MAPLE, the laser processed samples were compared with equivalent dropcast samples by IRM analysis, in terms of purity and stoichiometry (IR spectra), as well as structural integrity and efficient laser transfer (IR maps). For all specimens, IR spectra were recorded for different points on each sample, while the IR maps were built by monitoring the distribution of absorption bands from  $\sim 1750 \text{ cm}^{-1}$  and  $\sim 2990 \text{ cm}^{-1}$ , corresponding to carbonyl (C=O) and methyl (-CH<sub>3</sub>) groups, respectively. Colors from each IR map are directly related to the monitored absorption band's intensity, ranging from blue to red (minimum to maximum absorbance intensity, respectively).

The IR spectroscopy was employed in order to obtain important data on the chemical preservation and stoichiometric transfer of PLA/ $\text{Fe}_3\text{O}_4@\text{EG}$  material during the laser-assisted synthesis of thin films. For the dropcast sample, the IR spectrum (corresponding to the initial material) is depicted in Figure 7. Specific absorbance maxima in the composite sample are identified as corresponding to the following functional groups from both organic compounds:  $\sim 2995 \text{ cm}^{-1}$  and  $\sim 2945 \text{ cm}^{-1}$  (asymmetric and symmetric stretching of -CH<sub>3</sub>),  $\sim 1753 \text{ cm}^{-1}$  (strong stretching of C=O),  $\sim 1453 \text{ cm}^{-1}$  (overlapped bending of C-H and C=O) and  $\sim 1089 \text{ cm}^{-1}$  (stretching of C-O) [93,94]. The IR peaks from  $\sim 1381 \text{ cm}^{-1}$  and  $\sim 1185 \text{ cm}^{-1}$  characterize bending of -CH<sub>3</sub> and asymmetric stretching of C-O-C from PLA [95,96]. Stretching vibrations of C-O originating from the cyclic ether of eucalyptol may be assigned at  $\sim 1268 \text{ cm}^{-1}$  [97,98].

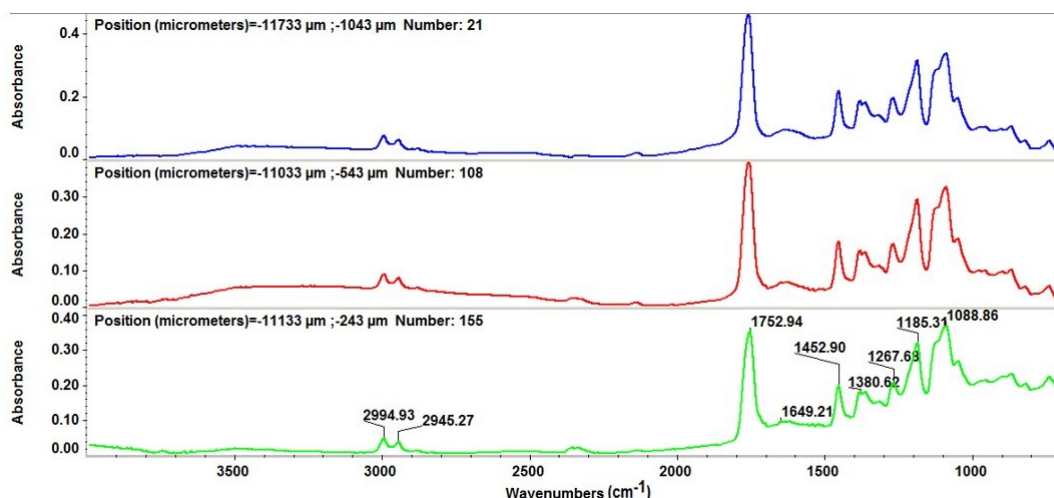


**Figure 7.** IR spectra of polylactic acid (PLA)/ $\text{Fe}_3\text{O}_4@\text{EG}$  dropcast.

By considering the color distribution from infrared maps (Figure 8, left) and its correlation with material's transfer, one can notice that the value of laser fluence has a clear impact on the homogeneity of obtained coatings, which is directly related to functional groups repartition. The lowest distribution of PLA/Fe<sub>3</sub>O<sub>4</sub>@EG material onto the substrates (predominantly blue and green areas) is identified for the 200 mJ/cm<sup>2</sup> laser fluence (Figure 8a, left), followed by the 400 mJ/cm<sup>2</sup> laser fluence (Figure 8c, left). In the first case, this outcome may be related to an inefficient material transfer, as the corresponding IR spectra (Figure 8a, right) evidence the presence of less intense (or even absent) absorbance maxima when compared to the dropcast sample. For the highest laser fluence, the IR spectra (Figure 8c, right) point out significant degradation of previously identified functional groups. The most homogenous and uniform transfer of PLA/Fe<sub>3</sub>O<sub>4</sub>@EG material is attained by using the 300 mJ/cm<sup>2</sup> laser fluence (Figure 8b, left), with no alterations in the chemical structure of composite material being observed (Figure 8b, right).

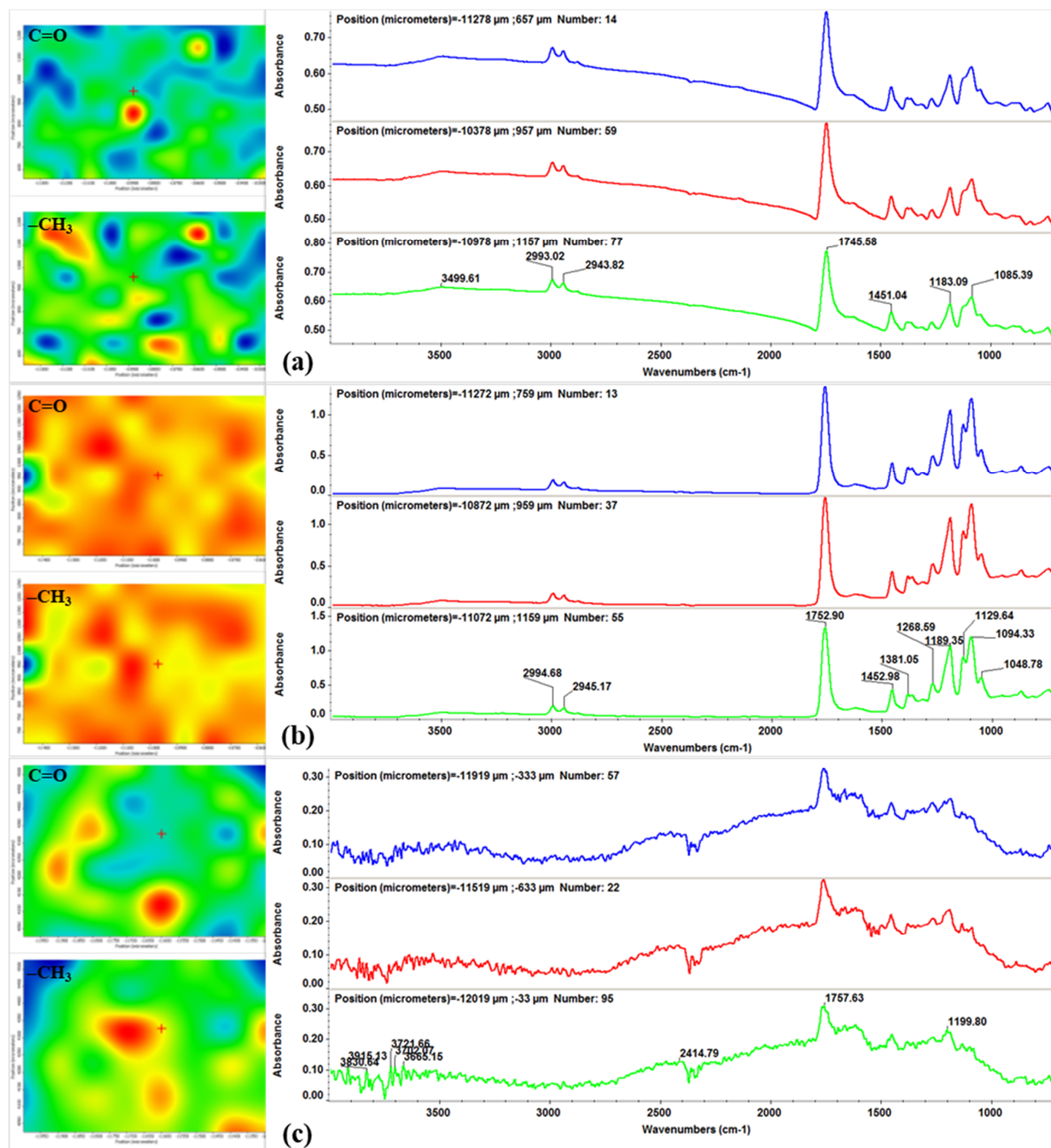


**Figure 8.** IR maps (left) and corresponding IR spectra (right) of PLA/Fe<sub>3</sub>O<sub>4</sub>@EG coatings processed by matrix-assisted pulsed laser evaporation (MAPLE) at 200 mJ/cm<sup>2</sup> (a), 300 mJ/cm<sup>2</sup> (b) and 400 mJ/cm<sup>2</sup> (c).

The infrared data confirm that composite coatings containing PLA and iron oxide nanoparticles conjugated with EG essential oil were successfully obtained. In terms of chemical integrity and efficient material transfer, the middle laser fluence ( $300 \text{ mJ/cm}^2$ ) was experimentally identified as the optimal choice for the MAPLE synthesis of PLA/Fe<sub>3</sub>O<sub>4</sub>@EG coatings. Therefore, composite materials for further characterization (SEM investigation) and cellular evaluation (biological and microbiological assays) were obtained only by using this particular value of laser fluence.

The surface morphology, structure and thickness of PLA/Fe<sub>3</sub>O<sub>4</sub>@EG samples obtained at  $300 \text{ mJ/cm}^2$  laser fluence were evaluated by the plain view and cross-section SEM analysis, respectively. The lower magnification image (Figure 9a) shows a uniform and complete coverage of the substrate by the composite material, with a particulate aspect (suggesting a highly irregular surface) and relatively homogenous aspect. The partial solubility of PLA in DMSO may be responsible for the formation of a continuous polymer layer (with predominant cavity-like structure) and the presence of spherical-shaped particulate structures (occurred due to intense reorganization of polymer following its interaction with the laser beam). At higher magnification (Figure 9b), one can notice that aggregates of Fe<sub>3</sub>O<sub>4</sub>@EG nanoparticles are embedded and uniformly distributed within the PLA matrix. The cross-section image from Figure 9c indicates a rough surface of PLA/Fe<sub>3</sub>O<sub>4</sub>@EG coating, which is a beneficial parameter for cellular interactions. The thickness of composite coating, with irregular surface morphology, ranges between 420 nm and 1.7  $\mu\text{m}$ .

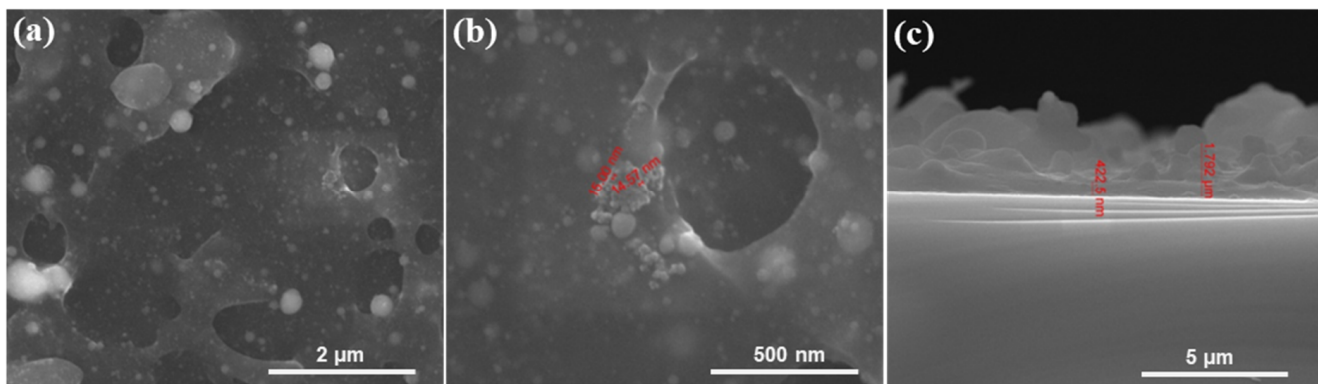


**Figure 9.** Plain view (a,b) and cross-section (c) scanning electron microscopy (SEM) micrographs of PLA/Fe<sub>3</sub>O<sub>4</sub>@EG coatings.

For the biological evaluation of PLA/Fe<sub>3</sub>O<sub>4</sub>@EG coatings, the percent of metabolically active stem cells incubated for 72 h in the presence of MAPLE processed samples was determined (Figure 10). The viability of AFSCs was calculated as reported to control cells (non-treated cells). The MTT assay results demonstrate that PLA/Fe<sub>3</sub>O<sub>4</sub>@EG coatings are favorable substrates for the normal development of AFSCs, since no modification in the metabolic activity of cells is evidenced after three days of treatment. In comparison with control specimens, a slightly decreased cellular viability (~3%) is noticed in the case of nanostructured composites, but the amount of viable cells is maintained above 92%. Besides their versatile composition and tunable characteristics (including mechanical and thermal response, permeability and solubility), the intrinsic biocompatibility and adjustable biodegradability of PLA-based biomaterials are essential aspects for the development of new and effective antimicrobial formulations [99–102]. The obtained biological results show that PLA/Fe<sub>3</sub>O<sub>4</sub>@EG coatings are highly biocompatible substrates for the normal growth and proliferation of human-derived cells and indicate them as suitable candidates for surface modification of mid-term implantable biomaterials and devices.

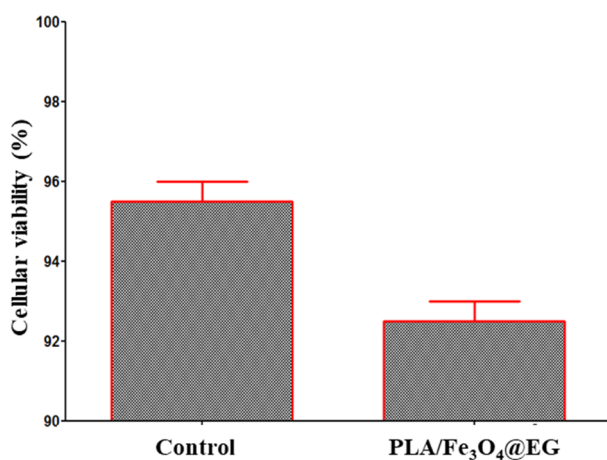


**Figure 10.** Viability results of human amniotic fluid-derived mesenchymal stem cells (AFSCs) incubated for 72 h in the presence of PLA/Fe<sub>3</sub>O<sub>4</sub>@EG coatings.

The ability of MAPLE processed nanostructured composite films to inhibit bacterial biofilm formation and maturation was evaluated at different time intervals against representative Gram-negative (*E. coli*) and Gram-positive (*S. aureus*) pathogens.

In the case of *E. coli* strain (Figure 11, left), PLA/Fe<sub>3</sub>O<sub>4</sub>@EG coatings determine the decrease of the bacterial population by ~2.5 folds, both after 24 h and 48 h of treatment. It can be clearly noticed that after 72 h of incubation in the presence of composite materials, the CFU/mL values are reduced by three times when compared to control values. Regarding the impact of PLA/Fe<sub>3</sub>O<sub>4</sub>@EG coatings on *S. aureus* biofilm development (Figure 11, right), the inhibition level is more evident, since bacterial populations are reduced by at least 10 folds, regardless of the incubation time. These overall results evidence the effectiveness of PLA/Fe<sub>3</sub>O<sub>4</sub>@EG composite films as anti-biofilm surfaces.

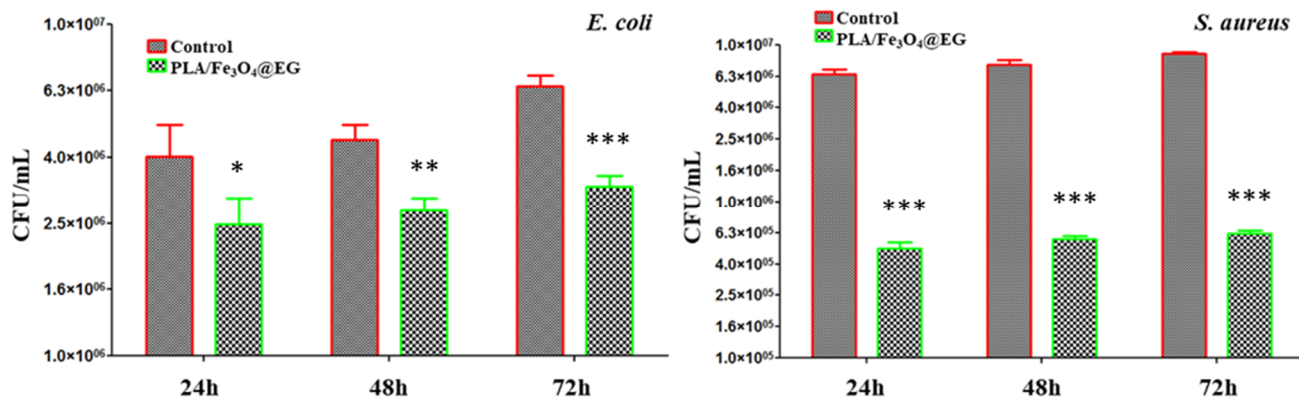


**Figure 11.** Microbial biofilm development of *E. coli* (left) and *S. aureus* (right) after different incubation periods with PLA/Fe<sub>3</sub>O<sub>4</sub>@EG coatings, expressed as CFU/mL values reflecting number of viable cells imbedded in biofilms. \*  $p < 0.05$ ; \*\*  $p < 0.01$ ; \*\*\*  $p < 0.001$  (CFU/mL values of control vs. PLA/Fe<sub>3</sub>O<sub>4</sub>@EG coatings).

As a general remark, the inhibition of biofilm development by PLA/Fe<sub>3</sub>O<sub>4</sub>@EG coatings is comparable for all investigated time intervals for both bacteria. Such behavior indicates the sustained efficiency of proposed nanostructured materials against microbial biofilm development, as they proved to interfere with the early stage formation of biofilms (contamination and colonization), but also with the maturation phase. The particular anti-biofilm effect evidenced against *S. aureus* relies on the compositional and microstructural differences between the cells of selected pathogens [103,104]. Although the exact antimicrobial mechanism is not known, we assume synergistic effects due to EO and magnetite nanoparticles, both with proved antimicrobial activity. The main antimicrobial mecha-

nism of *Eucalyptus globulus* EO is the membrane cell damage and interference with proton pumps and electrolyte channels [105,106]. On the other hand, magnetite nanoparticles are known for their cell wall damage properties, as well as stimulation of the intracellular release of reactive oxygen species (ROS), which interfere with vital mechanisms, such as cell division and signaling [107]. Improved antimicrobial activity of synthetic [108,109] and natural [110,111] antibiotics were reported when conjugated with magnetite nanoparticles.

Herein, the biological results evidence that PLA/Fe<sub>3</sub>O<sub>4</sub>@EG coatings are highly biocompatible substrates for human-derived cells. The microbiological data indicate that nanostructured PLA/Fe<sub>3</sub>O<sub>4</sub>@EG materials are suitable candidates for anti-biofilm surface modification of short-term to mid-term implantable biomaterials and devices.

#### 4. Conclusions

The present study reports the successful synthesis of PLA/Fe<sub>3</sub>O<sub>4</sub>@EG nanocomposite coatings and their potential use as biocompatible and anti-biofilm surfaces for implantable biomaterials and devices. By using a modified co-precipitation protocol, ultra-small ( $7.5 \pm 2.5$  nm) highly crystalline magnetite nanoparticles were conjugated with a natural antibiotic, Eucalyptus essential oil. The MAPLE technique provided an efficient, uniform and stoichiometric synthesis of nanostructured composite thin films. The cellular assays proved that the PLA/Fe<sub>3</sub>O<sub>4</sub>@EG coatings did not affect the viability and proliferation of eukaryote cells, while significantly interfered with the formation and maturation of bacterial biofilms. Thus, the proposed PLA/Fe<sub>3</sub>O<sub>4</sub>@EG nanocomposite coatings represent suitable candidates for surface modification of implantable biomaterials and devices by enhancing their biocompatibility and inducing or potentiating their anti-infective effects.

**Author Contributions:** Conceptualization, V.G. and A.M.G.; methodology, V.G., G.D.M., L.M., F.I., A.M.H. and A.M.G.; validation, G.D.M., L.M., F.I., A.M.H., B.S.V., A.C.B. and O.-C.O.; investigation, O.G., R.C.P., G.D.M., L.M., F.I., A.M.H., B.S.V., A.C.B. and O.-C.O.; resources, V.G., A.M.G. and E.A.; writing—original draft preparation, O.G., R.C.P.; writing—review and editing, O.G., V.G., R.C.P., F.I. and A.M.H.; visualization, V.G. and A.M.G.; supervision, L.M., A.M.G. and E.A.; and project administration, E.A. All authors have read and agreed to the published version of the manuscript.

**Funding:** This research received no external funding.

**Institutional Review Board Statement:** The study was conducted in compliance with the European Council Directive No. 86/609 (24 November 1986), the European Convention for the Protection of Vertebrate Animals used for Experimental and Other Scientific Purposes (2 December 2005) and the Romanian Parliament Law No. 43 on the protection of animals used for scientific purposes (11 April 2014). The study was approved by the Ethics Committee of the University of Medicine and Pharmacy of Craiova, Romania (Approval Report No. 118/27.05.2015).

**Informed Consent Statement:** Not applicable.

**Data Availability Statement:** The data presented in this study are available on request from the corresponding author.

**Acknowledgments:** This work was supported by the Romanian Ministry of Education and Research, under Romanian National Nucleu Program LAPLAS VI—contract no. 16N/2019. The authors acknowledge the support of the PN-III-P1-1.1-TE-2019-1506, project number 147TE/2020.

**Conflicts of Interest:** The authors declare no conflict of interest.

#### References

1. Cowan, M.M. Plant Products as Antimicrobial Agents. *Clin. Microbiol. Rev.* **1999**, *12*, 564–582. [[CrossRef](#)] [[PubMed](#)]
2. Efferth, T.; Xu, A.-L.; Lee, D.Y.W. Combining the wisdoms of traditional medicine with cutting-edge science and technology at the forefront of medical sciences. *Phytomedicine* **2019**, *64*, 153078. [[CrossRef](#)] [[PubMed](#)]
3. Yang, C.; Chen, H.; Chen, H.; Zhong, B.; Luo, X.; Chun, J. Antioxidant and Anticancer Activities of Essential Oil from Gannan Navel Orange Peel. *Molecules* **2017**, *22*, 1391. [[CrossRef](#)]
4. Manconi, M.; Petretto, G.; D’hallewin, G.; Escribano, E.; Milia, E.; Pinna, R.; Palmieri, A.; Firoznezhad, M.; Peris, J.E.; Usach, I.; et al. Thymus essential oil extraction, characterization and incorporation in phospholipid vesicles for the antioxidant/antibacterial treatment of oral cavity diseases. *Colloids Surf. B Biointerfaces* **2018**, *171*, 115–122. [[CrossRef](#)] [[PubMed](#)]

5. Uslu, M.E.; Mele, A.; Bayraktar, O. Evaluation of the hemostatic activity of Equisetum arvense extract: The role of varying phenolic composition and antioxidant activity due to different extraction conditions. *Biointerface Res. Appl. Chem.* **2019**, *9*, 4157–4163.
6. Sadeer, N.B.; Llorent-Martínez, E.J.; Bene, K.; Mahomoodally, M.F.; Mollica, A.; Sinan, K.I.; Stefanucci, A.; Ruiz-Riaguas, A.; Fernández-de Córdova, M.L.; Zengin, G. Chemical profiling, antioxidant, enzyme inhibitory and molecular modelling studies on the leaves and stem bark extracts of three African medicinal plants. *J. Pharm. Biomed. Anal.* **2019**, *174*, 19–33. [CrossRef] [PubMed]
7. Khammee, T.; Phoonan, W.; Ninsuwan, U.; Jaratrungtawee, A.; Kuno, M. Volatile constituents, in vitro and in silico anti-hyaluronidase activity of the essential oil from Gardenia carinata Wall. ex Roxb. flowers. *Biointerface Res. Appl. Chem.* **2019**, *9*, 4649–4654.
8. Abd El-Kaream, S.A. Biochemical and biophysical study of chemopreventive and chemotherapeutic anti-tumor potential of some Egyptian plant extracts. *Biochem. Biophys. Rep.* **2019**, *18*, 100637. [CrossRef]
9. Chen, X.; Zhang, L.; Qian, C.; Du, Z.; Xu, P.; Xiang, Z. Chemical compositions of essential oil extracted from Lavandula angustifolia and its prevention of TPA-induced inflammation. *Microchem. J.* **2020**, *153*, 104458. [CrossRef]
10. Selamoglu, Z.; Sevindik, M.; Bal, C.; Ozaltun, B.; Sen, I.; Pasdaran, A. Antioxidant, antimicrobial and DNA protection activities of phenolic content of Tricholoma virgatum (Fr.) P.Kumm. *Biointerface Res. Appl. Chem.* **2020**, *10*, 5500–5506.
11. Niu, G.; Li, W. Next-Generation Drug Discovery to Combat Antimicrobial Resistance. *Trends Biochem. Sci.* **2019**, *44*, 961–972. [CrossRef]
12. Podgoreanu, P.; Negrea, S.M.; Buia, R.; Delcaru, C.; Trusca, S.B.; Lazar, V.; Chifiriuc, M.C. Alternative strategies for fighting multidrug resistant bacterial infections. *Biointerface Res. Appl. Chem.* **2019**, *9*, 3834–3841.
13. Al Alawi, S.A.; Hossain, M.A.; Abusham, A.A. Antimicrobial and cytotoxic comparative study of different extracts of Omani and Sudanese Gum acacia. *Beni-Suef Univ. J. Basic Appl. Sci.* **2018**, *7*, 22–26. [CrossRef]
14. Kumari, R.; Mishra, R.C.; Sheoran, R.; Yadav, J.P. Fractionation of Antimicrobial Compounds from Acacia nilotica Twig Extract Against Oral Pathogens. *Biointerface Res. Appl. Chem.* **2020**, *10*, 7097–7105.
15. Yang, S.-K.; Yusoff, K.; Mai, C.-W.; Lim, W.-M.; Yap, W.-S.; Erin Lim, S.-H.; Lai, K.-S. Additivity vs Synergism: Investigation of the Additive Interaction of Cinnamon Bark Oil and Meropenem in Combinatory Therapy. *Molecules* **2017**, *22*, 1733. [CrossRef] [PubMed]
16. Lapinska, B.; Szram, A.; Zarzycka, B.; Grzegorczyk, J.; Hardan, L.; Sokolowski, J.; Lukomska-Szymanska, M. An In Vitro Study on the Antimicrobial Properties of Essential Oil Modified Resin Composite against Oral Pathogens. *Materials* **2020**, *13*, 4383. [CrossRef] [PubMed]
17. Cui, H.; Zhang, C.; Li, C.; Lin, L. Antimicrobial mechanism of clove oil on Listeria monocytogenes. *Food Control* **2018**, *94*, 140–146. [CrossRef]
18. Radünz, M.; Martins da Trindade, M.L.; Mota Camargo, T.; Radünz, A.L.; Dellinghausen Borges, C.; Avila Gandra, E.; Helbig, E. Antimicrobial and antioxidant activity of unencapsulated and encapsulated clove (*Syzygium aromaticum*, L.) essential oil. *Food Chem.* **2019**, *276*, 180–186. [CrossRef]
19. Behbahani, B.A.; Noshad, M.; Falah, F. Cumin essential oil: Phytochemical analysis, antimicrobial activity and investigation of its mechanism of action through scanning electron microscopy. *Microb. Pathog.* **2019**, *136*, 103716. [CrossRef] [PubMed]
20. Nazarpourvar, M.; Shakeri, A.; Ranjbariyan, A. Chemical Composition and Antimicrobial Activity Against Food Poisoning of Alcoholic Extract of *Nigella sativa* L. *Biointerface Res. Appl. Chem.* **2020**, *10*, 6991–7001.
21. Yuan, C.; Wang, Y.; Liu, Y.; Cui, B. Physicochemical characterization and antibacterial activity assessment of lavender essential oil encapsulated in hydroxypropyl-beta-cyclodextrin. *Ind. Crops Prod.* **2019**, *130*, 104–110. [CrossRef]
22. Kwiatkowski, P.; Łopusiewicz, Ł.; Kostek, M.; Drożłowska, E.; Pruss, A.; Wojciuk, B.; Sienkiewicz, M.; Zielińska-Bliźniewska, H.; Dołęgowska, B. The Antibacterial Activity of Lavender Essential Oil Alone and In Combination with Octenidine Dihydrochloride against MRSA Strains. *Molecules* **2020**, *25*, 95. [CrossRef] [PubMed]
23. Lu, M.; Dai, T.; Murray, C.K.; Wu, M.X. Bactericidal Property of Oregano Oil Against Multidrug-Resistant Clinical Isolates. *Front. Microbiol.* **2018**, *9*, 2329. [CrossRef]
24. Cui, H.; Zhang, C.; Li, C.; Lin, L. Antibacterial mechanism of oregano essential oil. *Ind. Crops Prod.* **2019**, *139*, 111498. [CrossRef]
25. Bajalan, I.; Rouzbahani, R.; Pirbalouti, A.G.; Maggi, F. Antioxidant and antibacterial activities of the essential oils obtained from seven Iranian populations of *Rosmarinus officinalis*. *Ind. Crops Prod.* **2017**, *107*, 305–311. [CrossRef]
26. Nakagawa, S.; Hillebrand, G.G.; Nunez, G. *Rosmarinus officinalis* L. (Rosemary) Extracts Containing Carnosic Acid and Carnosol are Potent Quorum Sensing Inhibitors of *Staphylococcus aureus* Virulence. *Antibiotics* **2020**, *9*, 149. [CrossRef]
27. Yazgan, H. Investigation of antimicrobial properties of sage essential oil and its nanoemulsion as antimicrobial agent. *LWT* **2020**, *130*, 109669. [CrossRef]
28. Popa, M.; Măruțescu, L.; Oprea, E.; Bleotu, C.; Kamerzan, C.; Chifiriuc, M.C.; Grădișteanu Pircalabioru, G. In Vitro Evaluation of the Antimicrobial and Immunomodulatory Activity of Culinary Herb Essential Oils as Potential Perioceutics. *Antibiotics* **2020**, *9*, 428. [CrossRef] [PubMed]
29. Khasru Parvez, A.; Saha, K.; Rahman, J.; Munmun, R.A.; Rahman, A.; Dey, S.K.; Rahman, S.; Islam, S.; Shariare, M.H. Antibacterial activities of green tea crude extracts and synergistic effects of epigallocatechingallate (EGCG) with gentamicin against MDR pathogens. *Heliyon* **2019**, *5*, e02126. [CrossRef]

30. Loose, M.; Pilger, E.; Wagenlehner, F. Anti-Bacterial Effects of Essential Oils against Uropathogenic Bacteria. *Antibiotics* **2020**, *9*, 358. [CrossRef] [PubMed]
31. Sakkas, H.; Economou, V.; Gousia, P.; Bozidis, P.; Sakkas, V.A.; Petsios, S.; Mpekoulis, G.; Ilia, A.; Papadopoulou, C. Antibacterial Efficacy of Commercially Available Essential Oils Tested Against Drug-Resistant Gram-Positive Pathogens. *Appl. Sci.* **2018**, *8*, 2201. [CrossRef]
32. Lorenzo-Leal, A.C.; Palou, E.; López-Malo, A. Evaluation of the efficiency of allspice, thyme and rosemary essential oils on two foodborne pathogens in in-vitro and on alfalfa seeds, and their effect on sensory characteristics of the sprouts. *Int. J. Food Microbiol.* **2019**, *295*, 19–24. [CrossRef] [PubMed]
33. Bachir, R.G.; Benali, M. Antibacterial activity of the essential oils from the leaves of *Eucalyptus globulus* against *Escherichia coli* and *Staphylococcus aureus*. *Asian Pac. J. Trop. Biomed.* **2012**, *2*, 739–742. [CrossRef]
34. Bugarin, D.; Grbović, S.; Orčić, D.; Mitić-Ćulafić, D.; Knežević-Vukčević, J.; Mimica-Dukić, N. Essential Oil of *Eucalyptus Gunnii* Hook. As a Novel Source of Antioxidant, Antimutagenic and Antibacterial Agents. *Molecules* **2014**, *19*, 19007–19020. [CrossRef]
35. Aldoghamim, F.S.; Flematti, G.R.; Hammer, K.A. Antimicrobial Activity of Several Cineole-Rich Western Australian *Eucalyptus* Essential Oils. *Microorganisms* **2018**, *6*, 122. [CrossRef] [PubMed]
36. Zengin, H.; Baysal, A.H. Antibacterial and Antioxidant Activity of Essential Oil Terpenes against Pathogenic and Spoilage-Forming Bacteria and Cell Structure-Activity Relationships Evaluated by SEM Microscopy. *Molecules* **2014**, *19*, 17773–17798. [CrossRef]
37. Aelenei, P.; Miron, A.; Trifan, A.; Bujor, A.; Gille, E.; Aprotosoaie, A.C. Essential Oils and Their Components as Modulators of Antibiotic Activity against Gram-Negative Bacteria. *Medicines* **2016**, *3*, 19. [CrossRef]
38. Elaissi, A.; Rouis, Z.; Mabrouk, S.; Bel Haj Salah, K.; Aouni, M.; Larbi Khouja, M.; Farhat, F.; Chemli, R.; Harzallah-Skhiri, F. Correlation Between Chemical Composition and Antibacterial Activity of Essential Oils from Fifteen *Eucalyptus* Species Growing in the Korbous and Jbel Abderrahman Arboreta (North East Tunisia). *Molecules* **2012**, *17*, 3044–3057. [CrossRef] [PubMed]
39. Ghaffar, A.; Yameen, M.; Kiran, S.; Kamal, S.; Jalal, F.; Munir, B.; Saleem, S.; Rafiq, N.; Ahmad, A.; Saba, I.; et al. Chemical Composition and in-Vitro Evaluation of the Antimicrobial and Antioxidant Activities of Essential Oils Extracted from Seven *Eucalyptus* Species. *Molecules* **2015**, *20*, 20487–20498. [CrossRef] [PubMed]
40. Abbasi, A.M.; Shah, M.H. Assessment of phenolic contents, essential/toxic metals and antioxidant capacity of fruits of *Viburnum foetens* decne. *Biointerface Res. Appl. Chem.* **2018**, *8*, 3178–3186.
41. Shetta, A.; Kegere, J.; Mamdouh, W. Comparative study of encapsulated peppermint and green tea essential oils in chitosan nanoparticles: Encapsulation, thermal stability, in-vitro release, antioxidant and antibacterial activities. *Int. J. Biol. Macromol.* **2019**, *126*, 731–742. [CrossRef] [PubMed]
42. Hadidi, M.; Pouramin, S.; Adinepour, A.; Haghani, S.; Jafari, S.M. Chitosan nanoparticles loaded with clove essential oil: Characterization, antioxidant and antibacterial activities. *Carbohydr. Polym.* **2020**, *236*, 116075. [CrossRef] [PubMed]
43. Hamed, A.; Zengin, G.; Aktumsek, A.; Selamoglu, Z.; Pasdar, A. In vitro and in silico approach to determine neuroprotective properties of iridoid glycosides from aerial parts of *Scrophularia amplexicaulis* by investigating their cholinesterase inhibition and anti-oxidant activities. *Biointerface Res. Appl. Chem.* **2020**, *10*, 5429–5454.
44. Noormand, F.; Kermani, A.S.; Raviz, E.K.; Esmaeilpour, K.; Golshani, M.; Bashiri, H.; Kalantaripour, T.P.; Asadi-Shekaari, M. Investigating the neuroprotective effects of Resveratrol on encephalopathy induced by bile duct ligation in male rats. *Biointerface Res. Appl. Chem.* **2020**, *10*, 5512–5515.
45. Liakos, I.L.; Iordache, F.; Carzino, R.; Scarpellini, A.; Oneto, M.; Bianchini, P.; Grumezescu, A.M.; Holban, A.M. Cellulose acetate—Essential oil nanocapsules with antimicrobial activity for biomedical applications. *Colloids Surf. B Biointerfaces* **2018**, *172*, 471–479. [CrossRef]
46. Das, S.; Horváth, B.; Šafranko, S.; Jokić, S.; Széchenyi, A.; Kőszegi, T. Antimicrobial Activity of Chamomile Essential Oil: Effect of Different Formulations. *Molecules* **2019**, *24*, 4321. [CrossRef] [PubMed]
47. Badea, M.L.; Iconaru, S.L.; Groza, A.; Chifiriuc, M.C.; Beuran, M.; Predoi, D. Peppermint Essential Oil-Doped Hydroxyapatite Nanoparticles with Antimicrobial Properties. *Molecules* **2019**, *24*, 2169. [CrossRef] [PubMed]
48. Ahmad, M.A.; Salmiati, S.; Marpongahtun, M.; Salim, M.R.; Lolo, J.A.; Syafiuddin, A. Green Synthesis of Silver Nanoparticles Using *Muntingia calabura* Leaf Extract and Evaluation of Antibacterial Activities. *Biointerface Res. Appl. Chem.* **2020**, *10*, 6253–6261.
49. Balaure, P.C.; Holban, A.M.; Grumezescu, A.M.; Mogoșanu, G.D.; Bălșeanu, T.A.; Stan, M.S.; Dinischiotu, A.; Volceanov, A.; Mogoantă, L. In vitro and in vivo studies of novel fabricated bioactive dressings based on collagen and zinc oxide 3D scaffolds. *Int. J. Pharm.* **2019**, *557*, 199–207. [CrossRef] [PubMed]
50. Amanzadi, B.; Mirzaei, E.; Hassanzadeh, G.; Mahdaviani, P.; Boroumand, S.; Abdollahi, M.; Abdolghaffari, A.H.; Majidi, R.F. Chitosan-based layered nanofibers loaded with herbal extract as wound-dressing materials on wound model studies. *Biointerface Res. Appl. Chem.* **2019**, *9*, 3979–3986.
51. Vasile, B.S.; Birca, A.C.; Musat, M.C.; Holban, A.M. Wound Dressings Coated with Silver Nanoparticles and Essential Oils for The Management of Wound Infections. *Materials* **2020**, *13*, 1682. [CrossRef] [PubMed]
52. Zubair, M.F.; Atolani, O.; Ibrahim, S.O.; Oguntoye, O.S.; Abdulrahim, H.A.; Oyegoke, R.A.; Olatunji, G.A. Chemical and biological evaluations of potent antiseptic cosmetic products obtained from *Momordica charantia* seed oil. *Sustain. Chem. Pharm.* **2018**, *9*, 35–41. [CrossRef]

53. Censi, R.; Vargas Peregrina, D.; Lacava, G.; Agas, D.; Lupidi, G.; Sabbieti, M.G.; Di Martino, P. Cosmetic Formulation Based on an Açaí Extract. *Cosmetics* **2018**, *5*, 48. [[CrossRef](#)]
54. Agarwal, P.; Tyagi, N.; Gaur, P.K.; Puri, D.; Shanmugam, S.K. Polyherbal anti acne gel containing extracts of *Mangifera indica* and *Syzygium cumini* seeds: Bioassay guided activity against *Propionibacterium acne*. *Biointerface Res. Appl. Chem.* **2019**, *9*, 4177–4182.
55. Arora, D.; Nanda, S. Quality by design driven development of resveratrol loaded ethosomal hydrogel for improved dermatological benefits via enhanced skin permeation and retention. *Int. J. Pharm.* **2019**, *567*, 118448. [[CrossRef](#)]
56. Pant, P.; Sut, S.; Castagliuolo, I.; Gandin, V.; Maggi, F.; Gyawali, R.; Dall’Acqua, S. Sesquiterpene rich essential oil from Nepalese Bael tree (*Aegle marmelos* (L.) Correa) as potential antiproliferative agent. *Fitoterapia* **2019**, *138*, 104266. [[CrossRef](#)] [[PubMed](#)]
57. Jabir, M.S.; Taha, A.A.; Sahib, U.I.; Taqi, Z.J.; Al-Shammari, A.M.; Salman, A.S. Novel of nano delivery system for Linalool loaded on gold nanoparticles conjugated with CALNN peptide for application in drug uptake and induction of cell death on breast cancer cell line. *Mater. Sci. Eng. C* **2019**, *94*, 949–964. [[CrossRef](#)]
58. Arzani, H.; Adabi, M.; Mosafir, J.; Dorkoosh, F.; Khosravani, M.; Maleki, H.; Nekounam, H.; Kamali, M. Preparation of curcumin-loaded PLGA nanoparticles and investigation of its cytotoxicity effects on human glioblastoma U87MG cells. *Biointerface Res. Appl. Chem.* **2019**, *9*, 4225–4231.
59. Asif, M.; Yehya, A.H.S.; Dahham, S.S.; Mohamed, S.K.; Shafaei, A.; Ezzat, M.O.; Majid, A.S.A.; Oon, C.E.; Majiddh, A.M.S.A. Establishment of in vitro and in vivo anti-colon cancer efficacy of essential oils containing oleo-gum resin extract of *Mesua ferrea*. *Biomed. Pharmacother.* **2019**, *109*, 1620–1629. [[CrossRef](#)] [[PubMed](#)]
60. Anghel, I.; Grumezescu, A.M.; Andronescu, E.; Anghel, A.G.; Ficai, A.; Saviuc, C.; Grumezescu, V.; Vasile, B.S.; Chifiriuc, M.C. Magnetite nanoparticles for functionalized textile dressing to prevent fungal biofilms development. *Nanoscale Res. Lett.* **2012**, *7*, 501. [[CrossRef](#)] [[PubMed](#)]
61. Geuli, O.; Metoki, N.; Zada, T.; Reches, M.; Eliaz, N.; Mandler, D. Synthesis, coating, and drug-release of hydroxyapatite nanoparticles loaded with antibiotics. *J. Mat. Chem. B* **2017**, *5*, 7819–7830. [[CrossRef](#)]
62. Ardekani, N.T.; Khorram, M.; Zomorodian, K.; Yazdanpanah, S.; Veisi, H.; Veisi, H. Evaluation of electrospun poly (vinyl alcohol)-based nanofiber mats incorporated with *Zataria multiflora* essential oil as potential wound dressing. *Int. J. Biol. Macromol.* **2019**, *125*, 743–750. [[CrossRef](#)]
63. Ebrahimpour, S.; Shahidi, S.B.; Abbasi, M.; Tavakoli, Z.; Esmaeili, A. Quercetin-conjugated superparamagnetic iron oxide nanoparticles (QCSPIONs) increases Nrf2 expression via miR-27a mediation to prevent memory dysfunction in diabetic rats. *Sci. Rep.* **2020**, *10*, 15957. [[CrossRef](#)] [[PubMed](#)]
64. Popescu, R.C.; Savu, D.; Dorobantu, I.; Vasile, B.S.; Hosser, H.; Boldeiu, A.; Temelie, M.; Stratificiu, M.; Iancu, D.A.; Andronescu, E.; et al. Efficient uptake and retention of iron oxide-based nanoparticles in HeLa cells leads to an effective intracellular delivery of doxorubicin. *Sci. Rep.* **2020**, *10*, 10530. [[CrossRef](#)]
65. Soleymani, M.; Khalighfard, S.; Khodayari, S.; Khodayari, H.; Kalhori, M.R.; Hadjighassem, M.R.; Shaterabadi, Z.; Alizadeh, A.M. Effects of multiple injections on the efficacy and cytotoxicity of folate-targeted magnetite nanoparticles as theranostic agents for MRI detection and magnetic hyperthermia therapy of tumor cells. *Sci. Rep.* **2020**, *10*, 1695. [[CrossRef](#)]
66. Afradi, N.; Foroughifar, N.; Qomi, M.; Pasdar, H. Folic acid-supported Fe<sub>3</sub>O<sub>4</sub> magnetic nanoparticles as a new, highly effective heterogeneous biocatalyst for the synthesis of 3,4-dihydropyrimidine thiones and their in vitro investigation as antibacterial active agents. *Biointerface Res. Appl. Chem.* **2018**, *8*, 3661–3669.
67. Szalai, A.J.; Manivannan, N.; Kapta, G. Super-paramagnetic magnetite nanoparticles obtained by different synthesis and separation methods stabilized by biocompatible coatings. *Colloids Surf. A Physicochem. Eng. Asp.* **2019**, *568*, 113–122. [[CrossRef](#)]
68. Sun, J.-Z.; Sun, Y.-C.; Sun, L. Synthesis of surface modified Fe<sub>3</sub>O<sub>4</sub> super paramagnetic nanoparticles for ultra sound examination and magnetic resonance imaging for cancer treatment. *J. Photochem. Photobiol. B Biol.* **2019**, *197*, 111547. [[CrossRef](#)]
69. Elazab, H.A.; El-Idreesy, T.T. Optimization of the catalytic performance of Pd/Fe<sub>3</sub>O<sub>4</sub> nanoparticles prepared via microwave-assisted synthesis for pharmaceutical and catalysis applications. *Biointerface Res. Appl. Chem.* **2019**, *9*, 3794–3799.
70. Samrot, A.V.; Sahithya, C.S.; Sruthi, D.P.; Selvarani, J.A.; Raji, P.; Prakash, P.; Ponnaiah, P.; Petchi, I.; Pattammadath, S.; Purayil, S.K.; et al. Itraconazole Coated Super Paramagnetic Iron Oxide Nanoparticles for Antimicrobial Studies. *Biointerface Res. Appl. Chem.* **2020**, *10*, 6218–6225.
71. Miguel, M.G.; Lourenço, J.P.; Faleiro, M.L. Superparamagnetic Iron Oxide Nanoparticles and Essential Oils: A New Tool for Biological Applications. *Int. J. Molec. Sci.* **2020**, *21*, 6633. [[CrossRef](#)] [[PubMed](#)]
72. Mihai, A.D.; Chircov, C.; Grumezescu, A.M.; Holban, A.M. Magnetite Nanoparticles and Essential Oils Systems for Advanced Antibacterial Therapies. *Int. J. Molec. Sci.* **2020**, *21*, 7355. [[CrossRef](#)]
73. Tirca, I.; Mitran, V.; Marascu, V.; Brajnicov, S.; Ion, V.; Stokker-Cheregi, F.; Popovici, I.A.; Cimpean, A.; Dinca, V.; Dinescu, M. In vitro testing of curcumin based composites coatings as antitumoral systems against osteosarcoma cells. *Appl. Surf. Sci.* **2017**, *425*, 1040–1051. [[CrossRef](#)]
74. Gherasim, O.; Grumezescu, A.M.; Grumezescu, V.; Iordache, F.; Vasile, B.S.; Holban, A.M. Bioactive Surfaces of Polylactide and Silver Nanoparticles for the Prevention of Microbial Contamination. *Materials* **2020**, *13*, 768. [[CrossRef](#)]
75. Chifiriuc, M.C.; Grumezescu, A.M.; Andronescu, E.; Ficai, A.; Cotar, A.I.; Grumezescu, V.; Bezirtzoglou, E.; Lazar, V.; Radulescu, R. Water dispersible magnetite nanoparticles influence the efficacy of antibiotics against planktonic and biofilm embedded *Enterococcus faecalis* cells. *Anaerobe* **2013**, *22*, 14–19. [[CrossRef](#)] [[PubMed](#)]

76. Grumezescu, A.M.; Cotar, A.I.; Andronescu, E.; Ficai, A.; Ghitulica, C.D.; Grumezescu, V.; Vasile, B.S.; Chifiriuc, M.C. In vitro activity of the new water-dispersible  $\text{Fe}_3\text{O}_4@\text{usnic}$  acid nanostructure against planktonic and sessile bacterial cells. *J. Nanopart. Res.* **2013**, *15*, 1766. [[CrossRef](#)]
77. Jiang, W.; Lai, K.L.; Hu, H.; Zeng, X.-B.; Lan, F.; Liu, F.; Liu, K.-X.; Wu, Y.; Gu, Z.-W. The effect of  $[\text{Fe}^{3+}]/[\text{Fe}^{2+}]$  molar ratio and iron salts concentration on the properties of superparamagnetic iron oxide nanoparticles in the water/ethanol/toluene system. *J. Nanopart. Res.* **2011**, *13*, 5135. [[CrossRef](#)]
78. Mayti, D.; Agrawal, D.C. Synthesis of Iron Oxide Nanoparticles under Oxidizing Environment and Their Stabilization in Aqueous and Non-Aqueous Media. *J. Magn. Magn. Mater.* **2007**, *308*, 46–55.
79. Sebastian, A.; Nangia, A.; Prasad, M.N.V. A green synthetic route to phenolics fabricated magnetite nanoparticles from coconut husk extract: Implications to treat metal contaminated water and heavy metal stress in *Oryza sativa* L. *J. Clean. Prod.* **2018**, *174*, 355–366. [[CrossRef](#)]
80. Bui, T.Q.; Ton, S.N.-C.; Duong, A.T.; Tran, H.T. Size-dependent magnetic responsiveness of magnetite nanoparticles synthesised by co-precipitation and solvothermal methods. *J. Sci. Adv. Mater. Dev.* **2018**, *3*, 107–112. [[CrossRef](#)]
81. Popescu, R.C.; Andronescu, E.; Vasile, B.S.; Trușcă, R.; Boldeiu, A.; Mogoantă, L.; Mogosanu, G.D.; Temelie, M.; Radu, M.; Grumezescu, A.M.; et al. Fabrication and Cytotoxicity of Gemcitabine-Functionalized Magnetite Nanoparticles. *Molecules* **2017**, *22*, 1080. [[CrossRef](#)]
82. Sirivat, A.; Paradee, N. Facile synthesis of gelatin-coated  $\text{Fe}_3\text{O}_4$  nanoparticle: Effect of pH in single-step co-precipitation for cancer drug loading. *Mater. Des.* **2019**, *181*, 107942. [[CrossRef](#)]
83. Ngwenya, S.; Guyo, U.; Zinyama, N.P.; Chigondo, F.; Nyamunda, B.C.; Muchanyereyi, N. Response surface methodology for optimization of  $\text{Cd(II)}$  adsorption from wastewaters by fabricated tartaric acid-maize tassel magnetic hybrid sorbent. *Biointerface Res. Appl. Chem.* **2019**, *9*, 3996–4005.
84. Popescu, R.C.; Stratuciuc, M.; Mustăcosu, C.; Temelie, M.; Trușcă, R.; Vasile, B.S.; Boldeiu, A.; Mirea, D.; Andrei, R.F.; Cenușă, C.; et al. Enhanced Internalization of Nanoparticles Following Ionizing Radiation Leads to Mitotic Catastrophe in MG-63 Human Osteosarcoma Cells. *Int. J. Mol. Sci.* **2020**, *21*, 7220. [[CrossRef](#)] [[PubMed](#)]
85. Rodrigues, V.H.; de Melo, M.M.R.; Tenberg, V.; Carreira, R.; Portugal, I.; Silva, C.M. Similarity analysis of essential oils and oleoresins of *Eucalyptus globulus* leaves produced by distinct methods, solvents and operating conditions. *Ind. Crops Prod.* **2021**, *164*, 113339. [[CrossRef](#)]
86. Kamel, S.; El-Gendy, A.A.; Hassan, M.A.; El-Sakhawy, M.; Kelnar, I. Carboxymethyl cellulose-hydrogel embedded with modified magnetite nanoparticles and porous carbon: Effective environmental adsorbent. *Carbohydr. Polym.* **2020**, *242*, 116402. [[CrossRef](#)] [[PubMed](#)]
87. Ebadi, M.; Buskaran, K.; Bullo, S.; Hussein, M.Z.; Fakurazi, S.; Pastorin, G. Synthesis and Cytotoxicity Study of Magnetite Nanoparticles Coated with Polyethylene Glycol and Sorafenib-Zinc/Aluminium Layered Double Hydroxide. *Polymers* **2020**, *12*, 2716. [[CrossRef](#)] [[PubMed](#)]
88. Shi, S.Q.; Che, W.; Liang, K.; Xia, C.; Zhang, D. Phase transitions of carbon-encapsulated iron oxide nanoparticles during the carbonization of cellulose at various pyrolysis temperatures. *J. Anal. Appl. Pyrol.* **2015**, *115*, 1–6. [[CrossRef](#)]
89. Lai, C.W.; Low, F.W.; Tai, M.F.; Hamid, S.B.A. Iron oxide nanoparticles decorated oleic acid for high colloidal stability. *Adv. Polym. Technol.* **2018**, *37*, 1712–1721. [[CrossRef](#)]
90. Bilcu, M.; Grumezescu, A.M.; Oprea, A.E.; Popescu, R.C.; Mogosanu, G.D.; Hristu, R.; Stanciu, G.A.; Mihailescu, D.F.; Lazar, V.; Bezirtzoglou, E.; et al. Efficiency of Vanilla, Patchouli and Ylang Ylang Essential Oils Stabilized by Iron Oxide@C14 Nanostructures against Bacterial Adherence and Biofilms Formed by *Staphylococcus aureus* and *Klebsiella pneumoniae* Clinical Strains. *Molecules* **2014**, *19*, 17943–17956. [[CrossRef](#)]
91. Temelie, M.; Popescu, R.C.; Cocioaba, D.; Vasile, B.S.; Savu, D. Biocompatibility study of magnetite nanoparticle synthesized using a green method. *Rom. J. Phys.* **2018**, *63*, 703.
92. Popescu, R.C.; Grumezescu, A.M. Nanoarchitectonics prepared by MAPLE for Biomedical Applications. In *Green Processes for Nanotechnology*; Basiuk, V.A., Basiuk, E.V., Eds.; Springer: Cham, Switzerland, 2015; pp. 303–325.
93. Alippilakkotte, S.; Kumar, S.; Sreejith, L. Fabrication of PLA/Ag nanofibers by green synthesis method using *Momordica charantia* fruit extract for wound dressing applications. *Colloids Surf. A Physicochem. Eng. Asp.* **2017**, *529*, 771–782. [[CrossRef](#)]
94. Obeizi, Z.; Benbouzid, H.; Ouchenane, S.; Yilmaz, D.; Culha, M.; Bououdina, M. Biosynthesis of Zinc oxide nanoparticles from essential oil of *Eucalyptus globulus* with antimicrobial and anti-biofilm activities. *Mater. Today Commun.* **2020**, *25*, 101553. [[CrossRef](#)]
95. Kumar, A.; Rao, T.V.; Chowdhury, S.R.; Reddy, S.V.S.R. Compatibility confirmation and refinement of thermal and mechanical properties of poly (lactic acid)/poly (ethylene-co-glycidyl methacrylate) blend reinforced by hexagonal boron nitride. *React. Funct. Polym.* **2017**, *117*, 1–9. [[CrossRef](#)]
96. Garakani, S.S.; Davachi, S.M.; Bagher, Z.; Esfahani, A.H.; Jenabi, N.; Atoufi, Z.; Khanmohammadi, M.; Abbaspourrad, A.; Rashedi, H.; Jalessi, M. Fabrication of chitosan/polyvinylpyrrolidone hydrogel scaffolds containing PLGA microparticles loaded with dexamethasone for biomedical applications. *Int. J. Biol. Macromol.* **2020**, *164*, 356–370. [[CrossRef](#)]
97. Pant, M.; Dubey, S.; Patanjali, P.K.; Naik, S.N.; Sharma, S. Insecticidal activity of eucalyptus oil nanoemulsion with karanja and jatropha aqueous filtrates. *Int. Biodeter. Biodegrad.* **2014**, *91*, 119–127. [[CrossRef](#)]

98. Raita, M.S.; Iconaru, S.L.; Groza, A.; Cimpeanu, C.; Predoi, G.; Ghegoiu, L.; Badea, M.L.; Chifiriuc, M.C.; Marutescu, L.; Trusca, R.; et al. Multifunctional Hydroxyapatite Coated with Arthemisia absinthium Composites. *Molecules* **2020**, *25*, 413. [[CrossRef](#)] [[PubMed](#)]
99. Cui, S.; Sun, X.; Li, K.; Gou, D.; Zhou, Y.; Hu, J.; Liu, Y. Polylactide nanofibers delivering doxycycline for chronic wound treatment. *Mater. Sci. Eng. C* **2019**, *104*, 109745. [[CrossRef](#)] [[PubMed](#)]
100. Mania, S.; Partyka, K.; Pilch, J.; Augustin, E.; Cieślik, M.; Ryl, J.; Jinn, J.-R.; Wang, Y.-J.; Michałowska, A.; Tylingo, R. Obtaining and Characterization of the PLA/Chitosan Foams with Antimicrobial Properties Achieved by the Emulsification Combined with the Dissolution of Chitosan by CO<sub>2</sub> Saturation. *Molecules* **2019**, *24*, 4532. [[CrossRef](#)] [[PubMed](#)]
101. Martin, V.; Ribeiro, I.A.; Alves, M.M.; Gonçalves, L.; Claudio, R.A.; Grenho, L.; Fernandes, M.H.; Gomes, P.; Santos, C.F.; Bettencourt, A.F. Engineering a multifunctional 3D-printed PLA-collagen-minocycline-nanoHydroxyapatite scaffold with combined antimicrobial and osteogenic effects for bone regeneration. *Mater. Sci. Eng. C* **2019**, *101*, 15–26. [[CrossRef](#)]
102. El-Naggar, M.E.; Al-Joufi, F.; Anwar, M.; Attia, M.F.; El-Bana, M.A. Curcumin-loaded PLA-PEG copolymer nanoparticles for treatment of liver inflammation in streptozotocin-induced diabetic rats. *Colloids Surf. B Biointerfaces* **2019**, *177*, 389–398. [[CrossRef](#)]
103. Luís, A.; Neiva, D.; Pereira, H.; Gominho, J.; Domingues, F.; Duarte, A.P. Stumps of Eucalyptus globulus as a Source of Antioxidant and Antimicrobial Polyphenols. *Molecules* **2014**, *19*, 16428–16446. [[CrossRef](#)] [[PubMed](#)]
104. Quatrin, P.M.; Verdi, C.M.; Ebbling de Souza, M.; Nunes de Godoi, S.; Klein, B.; Gundel, A.; Wagner, R.; de Almeida Vaucher, R.; Ferreira Ourique, A.; Santos, R.C.V. Antimicrobial and antibiofilm activities of nanoemulsions containing Eucalyptus globulus oil against *Pseudomonas aeruginosa* and *Candida* spp. *Microb. Pathog.* **2017**, *112*, 230–242. [[CrossRef](#)] [[PubMed](#)]
105. Swamy, M.K.; Akhtar, M.S.; Sinniah, U.R. Antimicrobial Properties of Plant Essential Oils against Human Pathogens and Their Mode of Action: An Updated Review. *Evid. Based Complement Altern. Med.* **2016**, *2016*, 21. [[CrossRef](#)] [[PubMed](#)]
106. Clavijo-Romero, A.; Quintanilla-Carvajal, M.X.; Ruiz, Y. Stability and antimicrobial activity of eucalyptus essential oil emulsions. *Food Sci. Technol. Int.* **2019**, *25*, 24–37. [[CrossRef](#)] [[PubMed](#)]
107. Gabrielyan, L.; Badalyan, H.; Gevorgyan, V.; Trchounian, A. Comparable antibacterial effects and action mechanisms of silver and iron oxide nanoparticles on *Escherichia coli* and *Salmonella typhimurium*. *Sci. Rep.* **2020**, *10*, 13145. [[CrossRef](#)] [[PubMed](#)]
108. Cotar, A.I.; Grumezescu, A.M.; Huang, K.S.; Voicu, G.; Chifiriuc, C.M.; Radulescu, R. Magnetite nanoparticles influence the efficiency of antibiotics against biofilm embedded *Staphylococcus aureus* cells. *Biointerface Res. Appl. Chem.* **2013**, *3*, 559–565.
109. Armijo, L.M.; Wawrzyniec, S.J.; Kopciuch, M.; Brandt, Y.I.; Rivera, A.C.; Withers, N.J.; Cook, N.C.; Huber, L.; Monson, T.C.; Smyth, H.D.C.; et al. Antibacterial activity of iron oxide, iron nitride, and tobramycin conjugated nanoparticles against *Pseudomonas aeruginosa* biofilms. *J. Nanobiotechnol.* **2020**, *18*, 35. [[CrossRef](#)]
110. Grumezescu, A.M.; Vasile, B.S.; Holban, A.M. Eugenol functionalized magnetite nanostructures used in anti-infectious therapy. *Lett. Appl. NanoBioSci.* **2013**, *2*, 120–123.
111. Atoche-Medrano, J.J.; León-Felix, L.; Faria, F.S.E.D.V.; Rodríguez, A.F.R.; Cunha, R.M.; Aragón, F.H.; Sousa, M.H.; Coaquira, J.A.H.; Azevedo, R.B.; Morais, P.C. Magnetite-based nanobioplatform for site delivering Croton cajucara Benth essential oil. *Mater. Chem. Phys.* **2018**, *207*, 243–252. [[CrossRef](#)]